

Dynamics of electron density, spin-phonon coupling, and dielectric properties of SmFeO₃ nanoparticles at the spin-reorientation temperature: Role of exchange striction

Smita Chaturvedi,¹ Priyank Shyam,¹ Amey Apte,^{1,*} Jitender Kumar,¹ Arpan Bhattacharyya,²
A. M. Awasthi,³ and Sulabha Kulkarni^{1,†}

¹Indian Institute of Science Education and Research, Pune, Dr. Homi Bhabha Road, Pashan, Pune, India

²Saha Institute of Nuclear Physics, 1/AF Bidhannagar, Kolkata, India

³UGC-DAE Consortium for Scientific Research, University Campus, Khandwa Road, Indore, India

(Received 29 January 2016; revised manuscript received 22 March 2016; published 26 May 2016)

Samarium orthoferrite (SmFeO₃) has been the subject of debate on the existence or nonexistence of ferroelectric properties. It has a high spin-reorientation transition temperature T_{SR} (480 K). Detailed synchrotron x-ray diffraction and Raman spectroscopy dielectric investigations in the 300 to 600 K temperature range of SmFeO₃ nanoparticles (~65 nm) have been performed. Raman spectroscopy established the existence of strong spin-phonon coupling and magnetostriction in the system. Magnetic measurements showed a spin-reorientation transition region from 480 to 450 K similar to that of a single crystal. The dielectric constant confirmed a clear anomaly around T_{SR} . The signature of unusual relaxor ferroelectric behavior in SmFeO₃ nanoparticles from 380 to 480 K was observed in the dielectric properties. The electron density plots obtained using Rietveld refinement of the synchrotron x-ray diffraction data showed the displacement of the Sm and Fe ions, which can play a key role in the anomalous behavior at T_{SR} . The analysis indicated the presence of magnetoelectric coupling due to the exchange interaction between Sm and Fe spins in SmFeO₃ nanoparticles.

DOI: 10.1103/PhysRevB.93.174117

I. INTRODUCTION

Magnetism and ferroelectricity are not usually expected to go hand in hand [1]. This makes the existence of multiferroicity in a material challenging. Therefore, there has been great interest among the scientific community for more than a decade to understand the fascinating mechanism of the coexistence of more than one ferroic order in a material [1–4]. Perovskite rare earth orthoferrites ($R\text{FeO}_3$: where R = lanthanide) are gaining attention due to their unusual structure, magnetic anisotropy and physical properties [4–7]. $R\text{FeO}_3$ perovskites are often orthorhombically distorted ($Pbnm/Pnma$) from the ideal cubic crystal lattice ($Pm-3m$) to a lower symmetry. This structural distortion influences the magnetic ordering and spin state transitions [8]. The anisotropic nature of rare earth and Fe moments gives rise to temperature-dependent structural and magnetic phase transitions. It is also established that their magnetic properties are sensitive to temperature, besides magnetic field, and photoinduction [4].

Samarium orthoferrite (SmFeO₃, or SFO) is a member of the $R\text{FeO}_3$ family that has been reported to have extraordinary device applications based on highest spin switching ($T_{SSW} = 278.5$ K) and high spin-reorientation transition ($T_{SR} = 480$ K) temperatures among the $R\text{FeO}_3$ family [9]. The spin-reorientation temperature T_{SR} is of great significance in terms of magnetoelastic devices, where anomalous magnetic, magnetoelectric, and magnetostriction characteristics near the spin-reorientation temperature can be used [10,11]. The spontaneous switching and reorientation of the spins of the Fe ions is a transition from one weakly ferromagnetic (FM) state to another, with change of the spin orientation from the c to the a axis of the rhombic crystal ($G_x F_z$ to $G_z F_x$) [12].

SFO has an orthorhombic structure ($Pnma/D_{2h}^{16}$ space group) and is composed of four distorted perovskite unit cells, as shown in Fig. 1. Structural studies using x-ray diffraction (XRD) in SFO have revealed a weak distortion of FeO₆ octahedra, leading to a buckling angle (Fe-O-Fe) of 147° in SFO [13].

So far, SFO has been studied mostly for its unusual magnetic, magneto-optical and electronic properties, in its bulk, polycrystalline, and single crystal forms, by various groups [14–19]. In 2011 and 2012, Lee *et al.* reported the improper ferroelectricity with a substantial degree of polarization. This surprising result was based on their experiments on single crystals of SFO and *ab initio* calculations [20,21]. They attributed these observations to reverse Dzyaloshinskii-Moriya (D-M) interaction over exchange interaction. In 2012 Johnson *et al.*, based on their analysis of SFO using group theory, argued against the existence of ferroelectricity due to reverse D-M interaction and suggested that there is a possibility of exchange striction between Sm and Fe ions [22]. Following this Lee *et al.* reconsidered their findings and attributed the origin of improper polarization [at the onset of paramagnetic to antiferromagnetic (AFM) transition T_N in a nonpolar system ($Pnma$)] to an exchange striction (magnetoelasticity) mechanism in the system. In 2014, Kuo *et al.* confirmed by performing powder and single crystal neutron diffraction, as well as complementary polarization-dependent soft x-ray absorption spectroscopy measurements on SFO single crystals, that a collinear AFM structure ($k = 0$, G type) is not compatible with inverse D-M interaction-driven ferroelectricity [23]. They confirmed (based on the structural data analysis of SFO single crystals) that there exists a clear sign for magnetoelastic coupling at the Néel temperature of ~675 K. The dielectric properties of SFO ceramics were reported by Prasad *et al.* in the frequency range of 100 Hz–1 MHz and in the temperature range from 80 to 300 K [24]. The colossal dielectric constant

*Present address: Rice University, Houston, Texas, USA.

†Corresponding author: s.kulkarni@iiserpune.ac.in

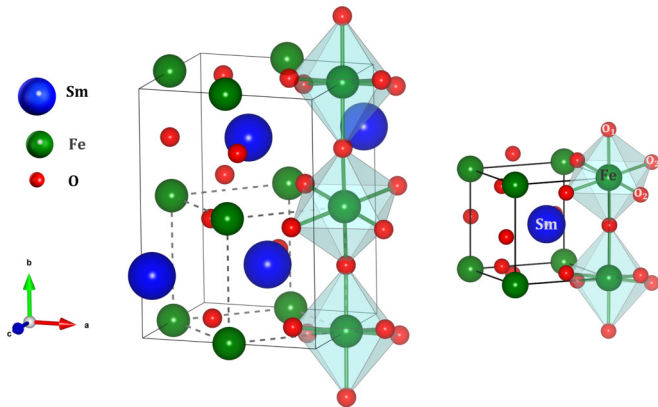


FIG. 1. A unit cell of SFO. Here, the red balls denote the oxygen atoms (O_1 and O_2), the blue balls represent the Sm atoms, and the green balls are used for the Fe atoms. The FeO_6 octahedra are shaded in light green to indicate the distortion in the $Pnma$ structure.

was found to be $\sim 10^4$ at room temperature. The response was similar to that observed for relaxor ferroelectrics [24]. Incidentally, Tokunaga *et al.* had earlier proposed that in other rare earth orthoferrite $DyFeO_3$ and $GdFeO_3$ single crystals, multiferroicity exists due to exchange interaction between rare earth and Fe spins [25,26].

Nanoparticles of SFO have also been reported. It has been shown that nanoparticles of SFO (particle size 150–300 nm) exhibit weak ferromagnetism due to canted AFM ordering and are semiconducting in nature [27,28]. Although structure and properties are closely related, to our knowledge there are no reports on the correlation between observed exchange striction driven ferroelectric relaxor-like feature of SFO and the dynamics of structural parameters, spin-phonon coupling, and dielectric properties near T_{SR} . Thus, many investigations that revolve around T_N of the single crystals and nanoparticles of SFO do not address T_{SR} and its impact or signature on the structural and dielectric parameters. The present paper is intended to investigate the effect of the spin-reorientation transition on the structural parameters, spin-phonon coupling, and dielectric properties of SFO. We observed a strong possibility of magnetoelectric coupling (MEC).

We have obtained XRD data at room temperature, as well as at various temperatures of interest, using synchrotron radiation. The lattice parameters obtained from such data are more promising than laboratory source data in terms of precision ($\sim 0.001 \text{ \AA}$). We used field-emission scanning electron microscopy (FESEM), energy dispersive analysis of x-rays (EDAX), high-temperature (300–645 K) synchrotron XRD, high-temperature (300–690 K) Raman spectroscopy techniques to characterize the nanoparticles and studied the dielectric properties (10 kHz–1 MHz) as a function of temperature (350–520 K). The high-temperature ranges are limited by the instrumentation used. We observed evidence of spin reorientation in structural and dielectric parameters at a spin-reorientation temperature T_{SR} of $\sim 480 \text{ K}$. We also observed that below T_{SR} the dielectric data shows ferroelectric relaxor-like behavior and above T_{SR} it vanishes. These studies indicate the contribution of exchange striction between Sm and Fe ions in SFO nanoparticles near T_{SR} .

II. EXPERIMENTAL DETAILS

A. Synthesis

SFO nanoparticles were synthesized using a similar soft chemical route combined with post-synthesis annealing, as reported earlier [29–32]. Briefly, it involves a reaction of stoichiometric amounts of $Sm(NO_3)_3 \cdot 5H_2O$ and $Fe(NO_3)_3 \cdot 9H_2O$ in the presence of tartaric acid at $T = 573 \text{ K}$. The precipitate was then heated in an oven at a temperature of 423 K. Samples were annealed at 773 K for 2 h. The annealed powder was washed in Milli-Q water and ethanol several times before complete drying.

B. Characterization

Scanning electron microscopy (SEM) images were recorded using a Zeiss Ultra Plus FESEM at a 3-kV operating voltage. For FESEM imaging, the samples were dispersed in ethanol, drop-cast on a silicon wafer, and dried under vacuum. EDAX is also obtained during FESEM. The elemental compositions of samarium and iron were determined by inductively coupled plasma-atomic emission spectrometry (ICP-AES) on a Spectro Arcos spectrometer. 0.1 g powder sample was dissolved in 10 mL of aqua regia solution, and this solution was used for ICP-AES analysis.

Synchrotron XRD measurements at room temperature and high temperature were carried out with x-ray beam of $E = 13.544 \text{ keV}$ ($\lambda = 0.9154 \text{ \AA}$) at BL-18B (Indian beamline), Photon Factory, KEK, Tsukuba, Japan. Energy of the x-ray beam was set by a Si (111) double crystal monochromator referenced against a Si standard (640b National Institute of Standards and Technology [NIST]). The diffraction patterns were recorded in a Bragg–Brentano geometry with a divergence slit ($\sim 300 \mu\text{m}$), an antiscattering slit ($\sim 350 \mu\text{m}$), and a receiving slit ($\sim 300 \mu\text{m}$). For the high-temperature measurements, the samples were loaded in a domed hot stage (DHS) 1100 heat cell (Anton Paar, Austria) covered with a dome-shaped, graphite x-ray window. Powder samples were placed on top of an aluminum nitride (AlN) ceramic base plate. Rietveld refinement of the XRD data was done using FullProf Suite. The high-temperature Raman spectra were recorded using Jobin Yvon HORIBA LabRAM HR visible micro Raman system, employing a He-Ne laser operating at 632.8 nm as the source in the backscattering geometry. The laser was focused to a spot of $\sim 2 \mu\text{m}$, and a $50\times$ objective lens was used for the collection of the scattered light. The samples were used in the pellet form for Raman measurements. The scattered light was analyzed using a single stage spectrograph charge-coupled device (CCD) detector. High-temperature magnetic measurements were performed between room temperature and 800 K using the oven attachment of the vibrating sample magnetometer (VSM) Physical Property Measurement System (PPMS) by Quantum Design Inc., San Diego, USA. In the oven option of the PPMS, the heater and the thermocouple were imprinted directly on the sample holder. The actual sample temperature, therefore, could be accurate only up to $\sim 20 \text{ K}$. The samples were loaded at room temperature under a nominal zero field, and the measurements were carried out while heating the samples under an applied magnetic field of 1 kOe. Dielectric measurements were carried out using an

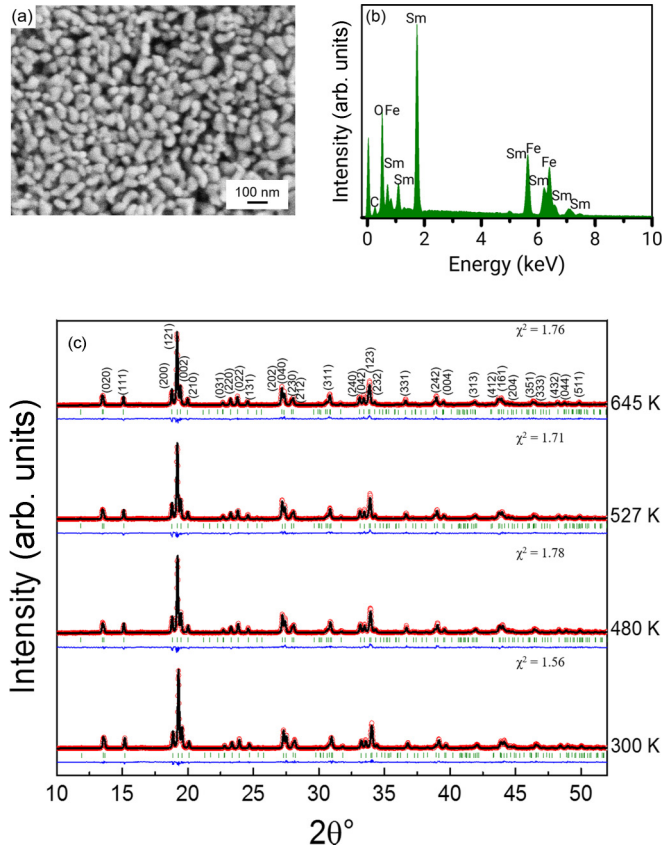


FIG. 2. (a) FESEM micrograph of SFO nanoparticles, (b) EDAX spectrum of SFO nanoparticles, and (c) Rietveld refined synchrotron XRD patterns of SFO nanoparticles at various temperatures of interest.

Alpha-A high-performance frequency analyzer (Novocontrol Technologies).

III. RESULTS AND DISCUSSION

A. FESEM and XRD

The FESEM micrographs shown in Fig. 2(a) indicate that the synthesized SFO sample has a particle size of ~ 65 nm. Figure 2(b) shows the EDAX spectrum of the sample, which gives the atomic composition as Sm (15.54%), Fe (15.54%), and O (68.93%). The ICP-AES analysis yielded a Sm:Fe ratio of 0.988, which is in agreement with the EDAX analysis. Rietveld refined room temperature and high-temperature powder XRD patterns of the sample recorded using synchrotron radiation are shown in Fig. 2(c). The diffraction lines are indexed based on the JCPDS Card No 00-039-1490, which confirms the orthorhombic ($Pnma$) symmetry of the synthesized sample over the investigated temperature range.

Unlike other rare earth orthoferrites, SFO is AFM at room temperature. Below T_N of ~ 680 K, the compound exhibits weak ferromagnetism only above room temperature [9]. In the temperature range 457–465 K, there is a second-order phase transition of the spin orientation in the $Pnma$ bc plane. The crystal becomes pure AFM at $T < 457$ K, with spins arranged along the [001] direction [33]. The structure of SFO comprises of network of corner-sharing FeO_6 octahedra and

is a rotationally distorted perovskite with Glazer's notation ($a^- b^+ a^-$) [34]. It is derived from the simple perovskite structure by two consequent rotations of FeO_6 octahedra: (1) around the [010] direction of the cubic perovskite sublattice and (2) around the [101] direction of the cubic perovskite sublattice [34].

Rietveld analysis of the synchrotron XRD data yielded accurate lattice parameters and atomic positions, which were used to define structural parameters. The effect of temperature on these is summarized in Fig. 3. Figure 3(a) shows lattice constants as a function of temperature.

It is observed that lattice constants a , b , and c and unit cell volume V increase with temperature due to lattice expansion. Figure 3(b) illustrates the variation of lattice distortion factors with temperature, while Fig. 3(c) shows average Fe-O1-Fe angle and tilt angle on the right y axis and orthorhombic strain on the left y axis as a function of temperature. Figure 3(d) shows the change in average Sm-O and average Fe-O bond lengths with temperature.

As shown in Fig. 3(a), the lattice parameters and volume (plotted as $V^{1/3}$) increase as we increase the temperature. The value of these structural parameters increases almost linearly, but there is a small shift from linearity at T_{SR} of ~ 480 K. The same behavior is observed in Fig. 3(b) for lattice distortion factors b/c and a/c plotted as a function of temperature.

Figure 3(c) shows the average tilt angle of FeO_6 octahedra φ and orthorhombic strain s as a function of temperature. These quantities are calculated as follows [35]:

$$\text{Spontaneous orthorhombic strain: } s_{(Pnma)} = \frac{2(a-c)}{(a+c)} \quad (1)$$

$$\text{Average tilt angle: } \varphi = \left(\frac{180^\circ - \langle \text{Fe-O-Fe} \rangle}{2} \right) \quad (2)$$

It is seen that the strain decreases as we increase the temperature. This indicates that the system is shifting toward higher symmetry. Here again, we see a slight deviation from linearity at T_{SR} of ~ 480 K in the curve. The average tilt angle φ of FeO_6 octahedra initially decreases with increasing temperature, until it reaches ~ 480 K, and then increases with increasing temperature as the temperature approaches Néel temperature. Figure 3(d) shows the evolution of average cation-anion bond lengths with temperature. Both average bond lengths (Sm-O)_{avg} and (Fe-O)_{avg} decrease from 300 to 480 K, and then they increase. It is observed here that the change in (Sm-O)_{avg} is greater than the change in (Fe-O)_{avg} bond lengths. This is because the average (Fe-O2) bond length does not vary much. While in the SmO_{12} dodecahedron, the averages of the (Sm-O1) and (Sm-O2) bond lengths change significantly. The cation-anion bond lengths and the cation-cation bond lengths are shown in Table I. In addition, the bond lengths in the FeO_6 octahedron and SmO_{12} dodecahedron at 300 K are shown in Fig. 4 for understanding of the respective lengths for Sm-O/Fe-O bond. All these changes in structural parameters in SFO nanoparticles around T_{SR} of ~ 480 K are pointing toward a clear signature of magnetic spin-reorientation transition. Table I also shows the bond lengths between Sm-Sm and Sm-Fe. For these cation-cation bond lengths, it is observed that their value increases with temperature and there is no

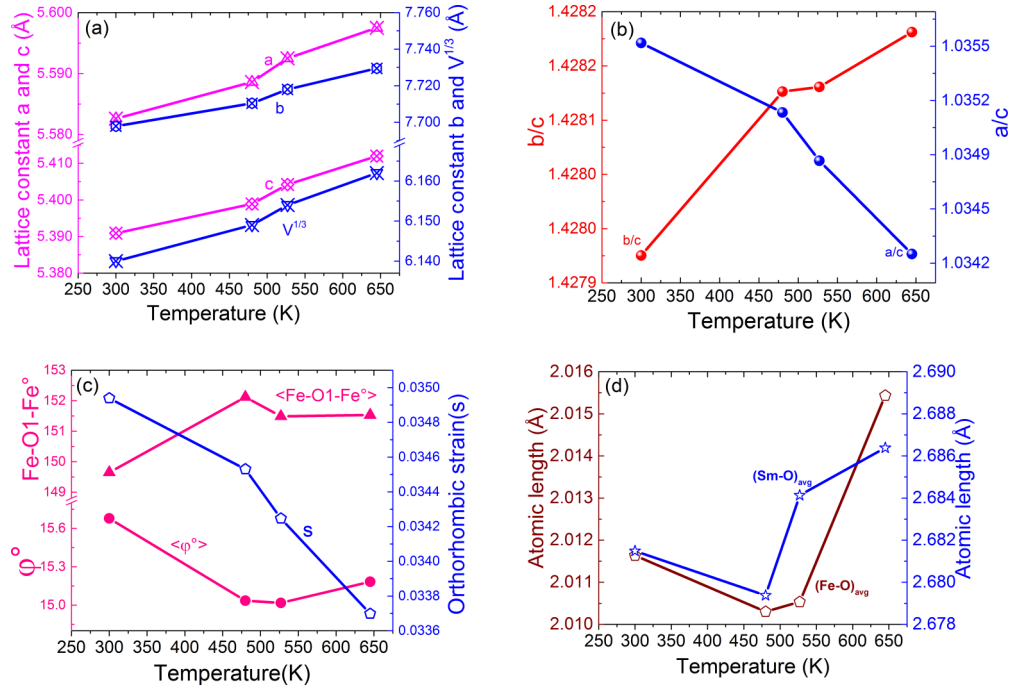


FIG. 3. (a) Lattice constants as a function of temperature, (b) variation of lattice distortion factors with temperature, (c) average tilt angle and orthorhombic strain as a function of temperature, and (d) change in average Sm-O and average Fe-O bond lengths with temperature.

anomaly with respect to spin-reorientation temperature. This indicates that Sm-O and Fe-O interactions play a significant role in reordering of spins of ~ 480 K.

TABLE I. Bond lengths between atoms of SFO nanoparticles obtained by Rietveld refinement of the synchrotron XRD data at various temperatures.

Bond between atoms	Bond length (\AA)			
	300 K	480 K	527 K	645 K
(Sm1)-(Sm1)	3.958(3)	3.964(4)	3.964(4)	3.964(4)
(Sm1)-(Sm1)	3.804(3)	3.808(4)	3.815(4)	3.824(4)
(Sm1)-(Sm1)	3.899(4)	3.905(4)	3.909(4)	3.913(4)
(Sm1)-(Fe1)	3.372(2)	3.377(3)	3.378(3)	3.38(3)
(Sm1)-(Fe1)	3.282(2)	3.286(3)	3.291(3)	3.298(3)
(Sm1)-(Fe1)	3.649(14)	3.652(14)	3.654(13)	3.653(14)
(Sm1)-(Fe1)	3.141(13)	3.147(13)	3.15(14)	3.158(13)
(Sm1)-(O1)	2.295(16)	2.309(17)	2.299(17)	2.297(17)
(Sm1)-(O1)	3.174(16)	3.139(17)	3.157(17)	3.163(17)
(Sm1)-(O1)	3.293(17)	3.201(17)	3.21(17)	3.201(17)
(Sm1)-(O1)	2.402(17)	2.489(17)	2.488(17)	2.5(17)
(Sm1)-(O2)	2.32(12)	2.321(11)	2.341(11)	2.33(12)
(Sm1)-(O2)	2.586(12)	2.609(11)	2.576(11)	2.59(12)
(Sm1)-(O2)	2.7(12)	2.687(11)	2.72(12)	2.723(12)
(Sm1)-(O2)	3.49(12)	3.493(11)	3.478(11)	3.49(12)
(Sm1)-(O2)	2.7(12)	2.687(11)	2.72(12)	2.723(12)
(Sm1)-(O2)	3.49(12)	3.493(11)	3.478(11)	3.49(12)
(Sm1)-(O2)	2.32(12)	2.321(11)	2.341(11)	2.33(12)
(Sm1)-(O2)	2.586(12)	2.609(11)	2.576(11)	2.59(12)
(Fe1)-(O1)	1.994(4)	1.986(4)	1.991(4)	1.994(4)
(Fe1)-(O2)	2.026(11)	2.029(11)	2.027(11)	2.044(11)
(Fe1)-(O2)	2.015(11)	2.016(11)	2.014(11)	2.009(11)

The symmetry of orthorhombic $R\text{FeO}_3$, does not allow piezoelectricity, where Fe^{3+} has no positional degree of freedom. However, magnetostriction is allowed in such compounds, regardless of symmetry [36]. Therefore, magnetoelastic coupling can be the root cause of nonlinearity of lattice parameters observed for SFO around T_{SR} . Nonlinear expansion across the spin-reorientation transition may evolve from temperature-induced spin excitations or canting in the vicinity of T_{SR} . Electrons with opposite spin will be subjected to stronger exchange-mediated Pauli repulsion, which would account for both the lattice expansion and the nonlinear anomalies observed at T_{SR} for SFO [36].

For $R\text{FeO}_3$ -type perovskites, the $Pnma$ structure maximizes coulombic attractive forces and minimizes ion-ion repulsion due to either increasing rare earth ionic radius or thermal expansion of the lattice [37]. As the unit cell volume of the $Pnma$ expands upon heating, the Sm^{3+} approaches the centrosymmetric position. This indicates a gradual reduction

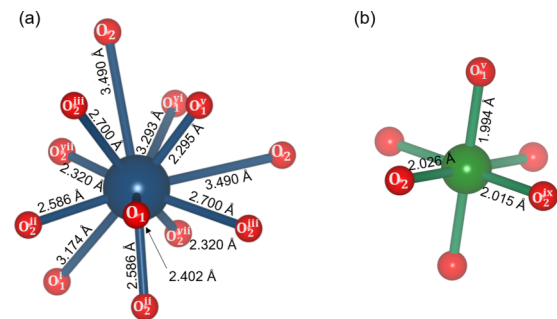


FIG. 4. Bond lengths in the SmO_{12} dodecahedron and FeO_6 octahedron at 300 K.

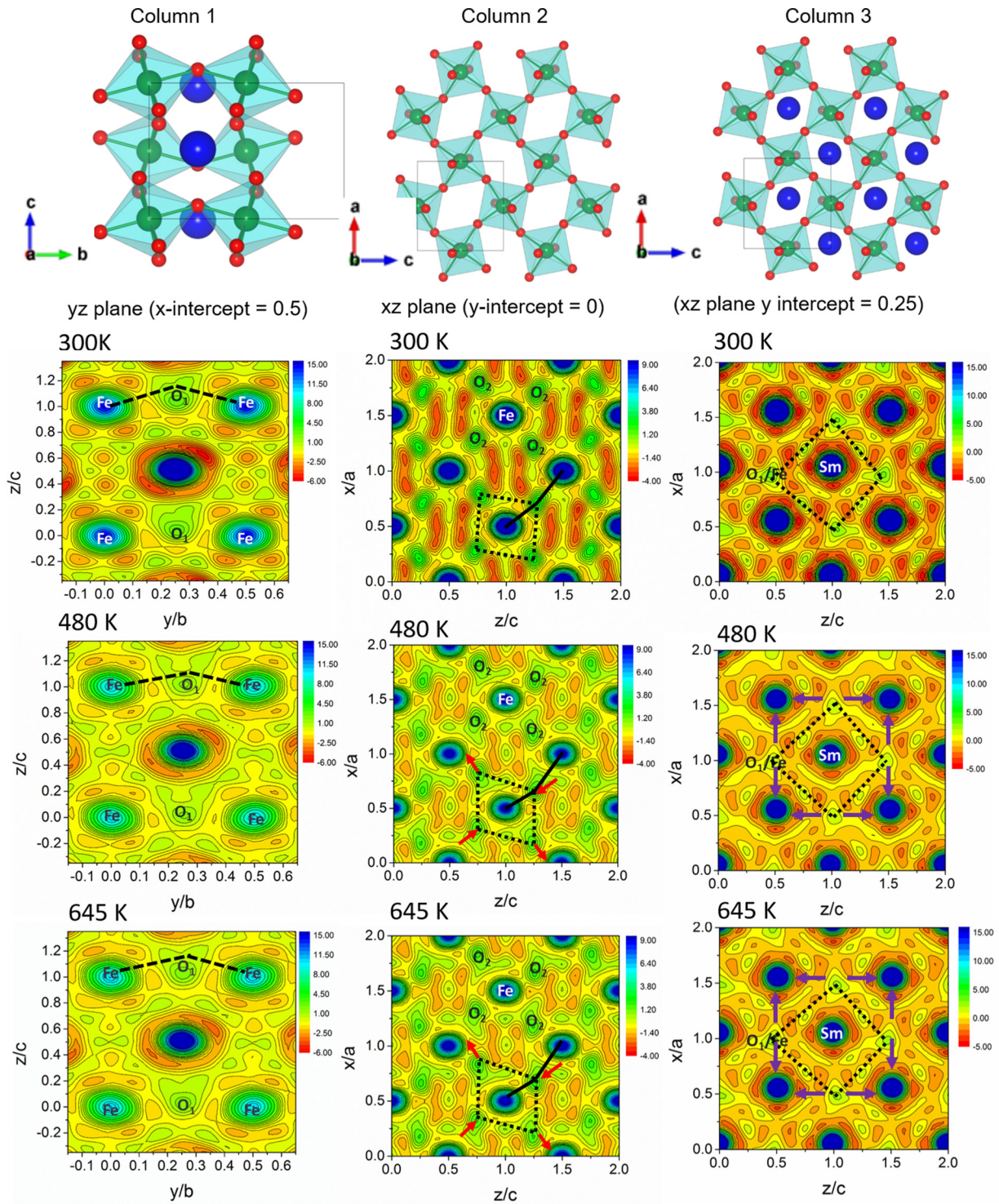


FIG. 5. The ED plots for SFO nanoparticles at room temperature (300 K), spin-reorientation temperature (480 K), and below Néel temperature (645 K) for the yz plane, x intercept = 0.5, in column 1; the xz plane, x intercept = 0, in column 2; and the xz plane, y intercept = 0.25, in column 3. The slice of the structure for the corresponding plane is shown in the top row of the figure for the one-to-one correspondence for anion and cations of the SFO system.

of the repulsive forces between ions with increasing temperature, eventually favoring higher symmetry over $Pnma$ structure.

Furthermore, the electron density (ED) maps of SFO nanoparticles are obtained from the refined XRD data. For

different planes of interest, appropriate intercepts have been obtained by Rietveld refinement of the synchrotron XRD data and are shown in Fig. 5 for room temperature (300 K), spin-reorientation temperature ($T_{SR} = 480$ K), and below Néel temperature (645 K) values.

The ED maps play significant role in understanding the interactions at the atomic level. The ED $\rho(x, y, z)$ is obtained from the reverse Fourier transform of the structure factors obtained from the Rietveld refinement, given as [38]

$$\rho(x, y, z) = \sum_{hkl} \frac{F_{hkl} \cdot e^{-2\pi i(hx+ky+lz)}}{V} \quad (3)$$

where $\rho(x, y, z)$ is the electron scattering density; F_{hkl} is the structure factor; h , k , and l are the Miller indices; and V is the volume of the unit cell.

Column 1 of Fig. 5 illustrates the sections of the ED in the yz plane taken at an x intercept of 0.5 for temperatures 300 to 645 K (top to bottom). Similarly, columns 2 and 3 show the ED on the xz plane taken at a y intercept of 0 and 0.25, respectively, for temperatures 300 to 645 K (top to bottom). At the top of each column, the corresponding section of the unit cell (for 300 K) is shown.

In column 1, we observe that as we move from 300 to 480 K, the ED near Fe atoms decreases (dark blue circles to lighter blue circles). Furthermore, the ED of Fe atoms increases slightly as we approach 645 K (blue circles). Then, at 300 K, the angle Fe-O1-Fe is at a minimum (149.65°), while at 480 K it increases (152.12°) and then at 645 K it again decreases slightly (151.53°). These observed changes can be explained as follows. At room temperature, the Fe^{3+} spins are oriented in the a direction; therefore, the corresponding maxima of ED of the Fe sublattice would be highlighted through the bc plane at $x = 0.5$. The decrease in ED of the Fe sublattice at 480 K can be attributed to the spin-reorientation transition of the FM vector of the Fe sublattice from an a direction to a c direction. [$\Gamma_2(G_z, F_x)$ to $\Gamma_4(G_x, F_z)$]. At T_{SR} , the spins order parallel to the c direction. Hence, the ED through the bc plane gives a less intense view of the ED of the Fe sublattice. At 645 K (below $T_{\text{N}} = 680$ K), SFO becomes a canted antiferromagnet with an FM vector from the Fe sublattice along the c axis, which gives a slight increase in the ED of the Fe sublattice. It is also observed that the ED between Sm and Fe atoms increases as we increase the temperature. This indicates the change in atomic positions of Sm and Fe atoms due to magnetic ordering and the spin reconfiguration of the Fe sublattice.

The sections in column 2 are taken such that the ED in the equatorial plane of the FeO_6 octahedra is evident. Here, there are three main observations. First, in this plane, the Fe-O2 bonds are visible and appear to form a rhombus composed of the Fe atom at the center and O_2 atoms at the vertices (see the black-dotted rhombus drawn to guide the eye in Fig. 5). The O_2 atoms connected along one diagonal are moving closer to the Fe atom at the center of the octahedra. Simultaneously, the O_2 atoms connected along the other diagonal are moving away from the Fe atom. As the temperature is increased to 480 K, the equatorial plane of the FeO_6 octahedra appears to change shape from a rhombus of almost equal diagonal lengths to a rhombus of unequal diagonal lengths.

Second, it is observed that the ED of Fe atoms is decreasing significantly at 480 K and decreases slightly again at 645 K (darker, bigger blue circle to smaller blue circles) with temperature. This indicates that the Fe atom is moving down in the b direction. At the same time, the low ED area (red) turns into a higher ED area (yellow) between any two octahedra.

This indicates that at 480 K, the distance from the O_2 atom of adjacent octahedra decreases. This also affirms the significant decrease of the calculated tilt angle at 480 K shown in Fig. 3(c).

The sections in column 3 depict the ED of the Sm sublattice with Fe/O1 ions. First, on increasing temperature above room temperature, the ED of the Sm ions or sublattice decreases at 480 K and then slightly increases at 645 K (bigger blue circle at 300 K to smaller blue circles at 480 K to slightly bigger blue circles at 645 K). Second, the ED of Fe/O1 ions decreases with temperature (green to yellow triangles). These two observations suggest that the distance between Sm-Fe and Sm-Sm ions is increasing. The Sm ion is being displaced from its position and is moving toward centrosymmetric position during the spin reorientation. This changes the dynamics of Sm-Fe ion interaction.

On the basis of overall analysis of the ED maps of SFO nanoparticles, it can be deduced that at T_{SR} , a nonlinear change in lattice parameters is observed. This can be attributed to the presence of exchange striction driven magnetoelasticity in the system. Furthermore, to relate and understand the effect of spin orientation on phonons and to explore the possibility of spin-phonon coupling in SFO nanoparticles, we have investigated the temperature-dependent Raman spectra of the sample.

B. Raman Spectroscopy

The changes in lattice distortion and magnetic structure are expected to be reflected in the change of phonon parameters near magnetic ordering temperature [39]. SFO crystallizes in an orthorhombically distorted perovskite $Pnma$, which is different from the ideal cubic perovskite $Pm\bar{3}m$ structure. This orthorhombic $Pnma$ structure is obtained by an antiphase tilt of the adjacent FeO_6 octahedra. The tilting of the FeO_6 octahedra gives rise to a distortion of the SmO_{12} dodecahedra. In the $Pnma$ structure, antiparallel A-cation displacements are permitted by symmetry [6,39]. The tilt, octahedra distortion, and A-cation displacement break the cubic symmetry and activate Raman modes [39]. According to group theory, the orthorhombic $Pnma$ structure with four formula units per unit cell give rise to 24 Raman-active modes ($\Gamma_{\text{Raman}} = 7A_g + 5B_{1g} + 7B_{2g} + 5B_{3g}$) [35].

Figure 6(a) shows the Raman spectra of SFO nanoparticles in the spectral range $100\text{--}700\text{ cm}^{-1}$ from room temperature to 690 K (beyond Néel temperature). Mode assignments have been done based on [34,40–42]. The phonon modes in SFO can be attributed to different symmetry operations: (1) those below 200 cm^{-1} are related to lattice modes involving Sm atom vibrations and (2) the modes in the region above 200 cm^{-1} consist of various modes involving vibrations of the Sm atom and oxygen. To be specific, (1) the $A_g(1)$ mode is related to the antisymmetric stretching vibrations of FeO_6 octahedra; (2) $B_{1g}(3)$, $A_g(2)$ are octahedral rotations around the crystallographic y axis and $B_{1g}(4)$, $A_g(4)$ are rotations around the x axis ($Pnma$ setting); (3) the singlet $A_g(7)$ in SFO is related to Sm-O vibrations; and (4) $B_{3g}(3)$ arises due to bending of FeO_6 octahedra.

Figure 6(b) shows the phonon frequency of modes $B_{2g}(5)$, $B_{1g}(3)$, $B_{1g}(4)$, and $A_g(7)$ as a function of temperature. It is observed that with increase in temperature, the phonon frequencies decrease up to T_{SR} (480 K); after a slight increase, they further decrease until T_{N} (680 K). This can be attributed

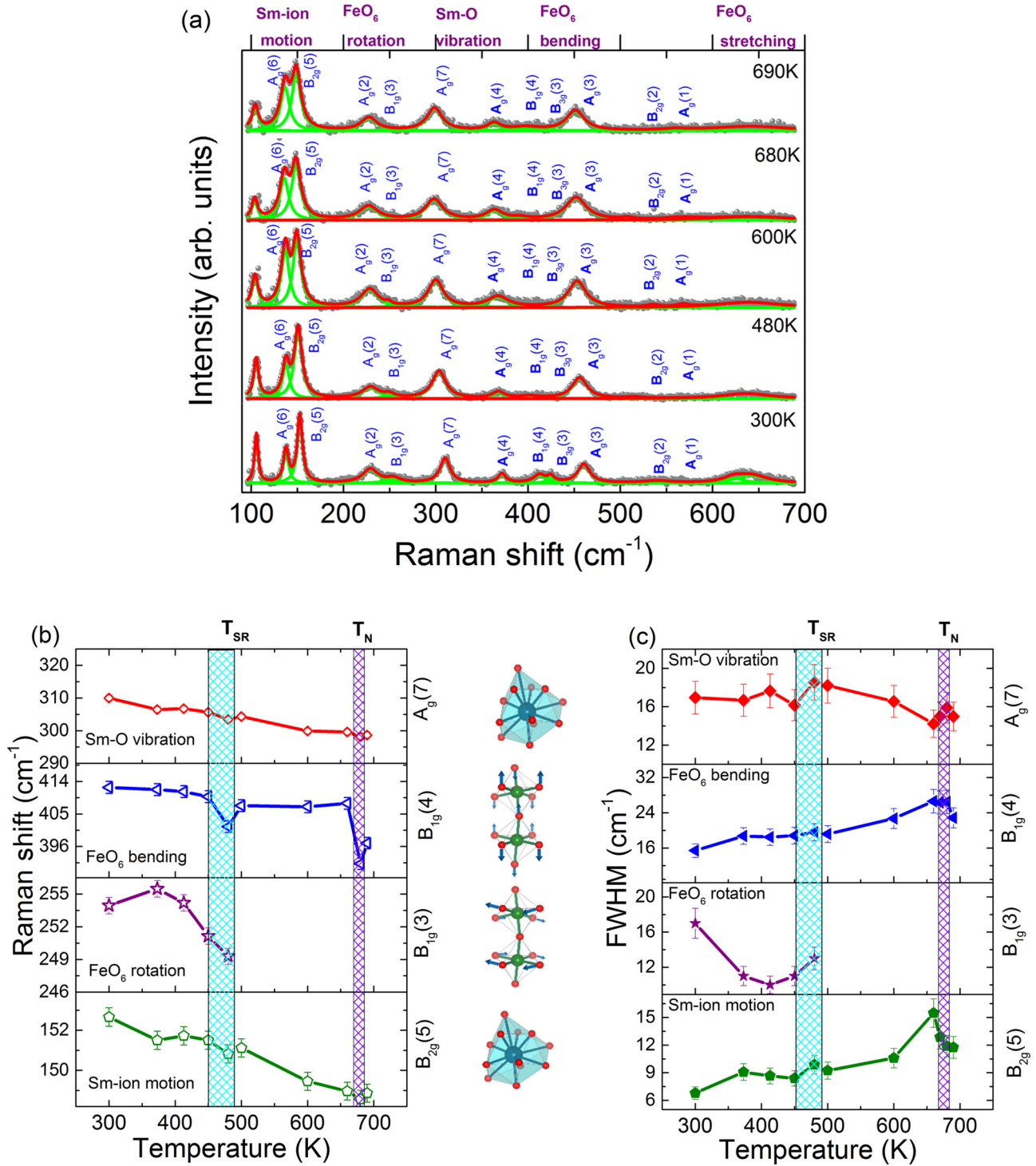


FIG. 6. (a) Raman spectra of SFO nanoparticles at various temperatures of interest; (b) Raman shift of modes $B_{2g}(5)$, $B_{1g}(3)$, $B_{1g}(4)$, and $A_g(3)$ plotted as a function of temperature; and (c) the full-width at half-maximum (FWHM) of modes $B_{2g}(5)$, $B_{1g}(3)$, $B_{1g}(4)$, and $A_g(3)$ plotted as a function of temperature.

to anharmonic effect and spin-phonon coupling [41]. The hardening of the modes around T_{SR} (480 K) and T_N (680 K) can be attributed to magnetostriction or lattice change [41,43].

In magnetic materials, the change in frequency (ω) of a phonon with temperature T is given by [43]

$$\Delta\omega(T) = (\Delta\omega)_{\text{latt}} + (\Delta\omega)_{\text{anh}} + (\Delta\omega)_{\text{ren}} + (\Delta\omega)_{\text{s-ph}} \quad (4)$$

where

$(\Delta\omega)_{\text{latt}}$ is the lattice expansion or contraction due to magnetostriction or anharmonicity effects.

$(\Delta\omega)_{\text{anh}}$ is the intrinsic anharmonic contribution—the anharmonic frequency shift at constant volume.

$(\Delta\omega)_{\text{ren}}$ is the effect of renormalization of the electronic states near the spin ordering temperature.

$(\Delta\omega)_{s-ph}$ is the spin-phonon contribution caused by the modulation of the exchange integral by lattice vibrations. Out of these four contributing factors, the third term $(\Delta\omega)_{ren}$ can be neglected if the carrier concentration is low.

The decrease in phonon frequencies is observed with increasing temperature up to T_N , along with an anomaly around T_{SR} , as shown in Fig. 6(b). This is attributed to the anharmonic effect [41]. Anharmonic frequency is given by the following relation:

$$\omega_{anh} = \omega_0 - C(1 + 2/(e^{\frac{\hbar\omega}{kT}} - 1)) \quad (5)$$

where ω_0 and C are adjustable parameters.

It is observed that phonon mode $B_{1g}(3)$ deviates from the above relation (5) below T_{SR} and disappears after T_{SR} . This could be attributed to combined contribution of quasi-harmonic effects and the spin-phonon coupling $((\Delta\omega)_{s-ph} + (\Delta\omega)_{lat})$. The frequency and corresponding linewidth of mode $A_g(7)$, which are derived from motion of Sm-O vibrations, show very small change with temperature. This suggests the existence of magnetostriction in the system.

The Raman linewidths are unaffected by a change in lattice volume caused by magnetostriction [41]. Hence, the relation of linewidth and temperature (compared to frequency and temperature) is more appropriate to confirm the existence of spin-phonon coupling in the system. Figure 6(c) shows the linewidth of modes $B_{2g}(5)$, $B_{1g}(3)$, $B_{1g}(4)$, and $A_g(7)$ as a function of temperature. It is observed from Fig. 6(c) that the linewidths increase with temperature until T_{SR} (480 K) and that after a slight increase (anomaly), they further decrease until T_N (680 K). Similar behavior is reported by Bhadram *et al.* for the rare earth orthochromites of magnetic R ions like Sm and Gd [41]. For nonmagnetic ions, this effect was found to be negligible. This indicates that these anomalies around T_{SR} and T_N are due to spin-phonon coupling.

Various structural changes observed in the detailed XRD analysis, which are a change in average tilt angle of octahedra with temperature, changes in Fe-O and Sm-O bond lengths, and displacement of Sm ion within the dodecahedron around T_{SR} , support the existence of spin-phonon coupling in SFO nanoparticles. The $A_g(7)$ mode shows a very small change in phonon frequency and an almost negligible change in phonon linewidths, which indicate the simultaneous presence of magnetostriction in the system.

Recently, Mochizuki *et al.* proposed a theoretical model establishing the crucial role of the spin-phonon coupling by considering $RMnO_3$, which is relevant to all multiferroic materials [44]. On correlating our system with the proposed model, it can be said that distorted intra- and interplane Fe-Fe and Sm-Fe interactions exist in SFO below T_{SR} and that this favors the displacement of Sm to minimize the distortion. In SFO, we observe strong spin-phonon coupling, unlike $RMnO_3$ due to weak FM Sm-Fe interactions, which cause the displacement of the magnetic Sm^{3+} ion. This displacement of Sm is confirmed by the Rietveld refinement and ED maps. It leads to the anomalous relaxor-like behavior of the system and can be explained by the exchange striction model shown in Fig. 7 [45]. The figure shows the dependence of the exchange striction on the atomic displacements. This displacement, in turn, drives appreciable polar lattice distortion, producing a relatively large polarization P . The exchange interaction

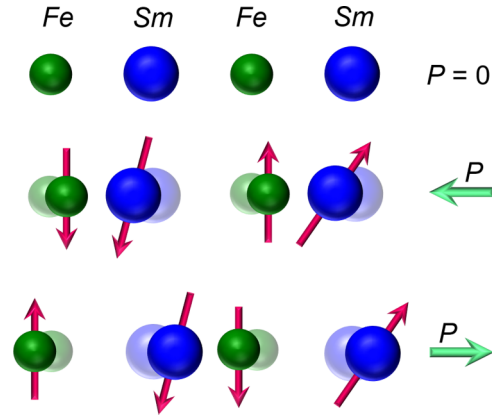


FIG. 7. Model depicting the mechanism of exchange striction responsible for ferroelectric-like behavior in SFO. Since the Sm ions order only at low temperature (~ 4 K), their moments are shown as randomly oriented. The Fe ions are AFM coupled below a T_N of ~ 680 K (not to scale).

is mediated between the Sm $4f$ moment and the Fe $3d$ moment.

C. Magnetic and Dielectric Measurements

In SFO, the Fe sublattice orders at $T_N = 670$ K with a weak canted FM moment along the c axis. At a spin-reorientation temperature T_{SR} of ~ 480 K, the Fe sublattice reorients from the c axis to the a axis [9]. At lower temperatures (below T_{SR}), the interactions between the Sm and the Fe ions dominate [9]. We performed χ - T measurements on SFO nanoparticles, and the corresponding results are presented in Fig. 8. We observe that the susceptibility increases drastically below $T_N = 670$ K, corresponding to the paramagnetic to AFM ordering of the Fe sublattice. The Néel temperature for SFO nanoparticles is comparable with that of single crystals [9,20,23].

Upon approaching the spin-reorientation temperature T_{SR} of ~ 480 K, a decrease in the susceptibility is observed in

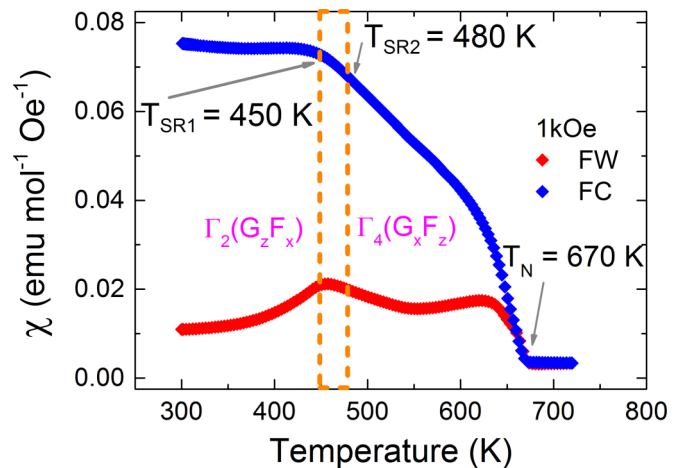


FIG. 8. Temperature dependence of susceptibility measured for FC and FW protocols for SFO nanoparticles showing spin reorientation from $\Gamma_2(G_z, F_x)$ to $\Gamma_4(G_x, F_z)$, corresponding to temperatures of 450 and 480 K, respectively.

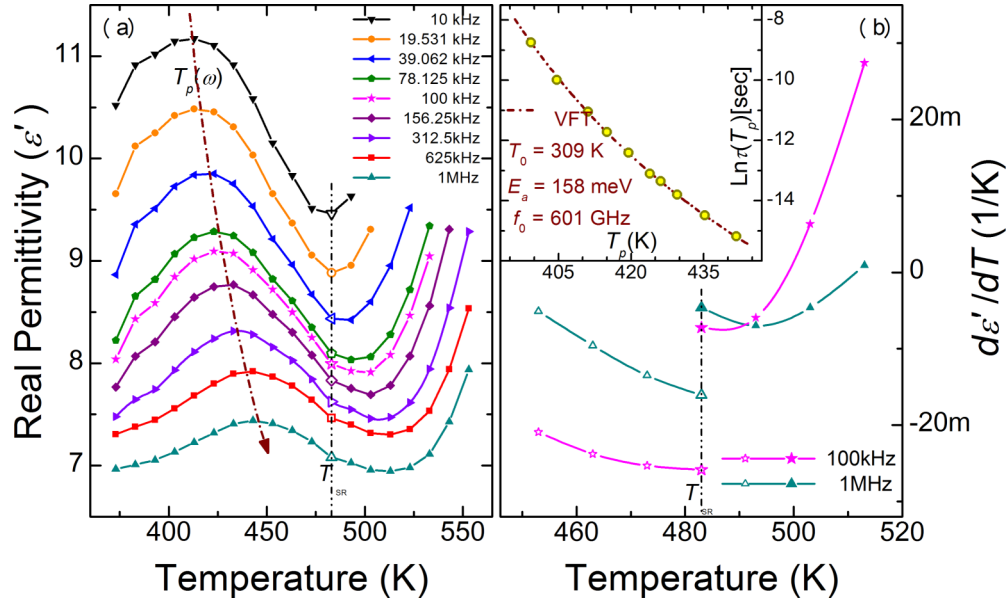


FIG. 9. (a) Real permittivity vs temperature across the spin reorientation transition, showing the anomaly at T_{SR} and a relaxor-like behavior (frequency-dependent maxima in real permittivity) below the T_{SR} . (b) A clear discontinuity in the slope across $T_{SR} = 483$ K. Inset in (b) shows relaxation times obtained from the peak frequency (across ~ 450 K) following VFT behavior, with finite freezing temperature $T_0 = 309$ K and activation energy $E_a = 158$ meV.

the field-warmed (FW) and field-cooled (FC) curves for SFO nanoparticles, shown in Fig. 8. In the spin-reorientation region, both curves show a decrease in susceptibility, which corresponds to second-order phase transition from $\Gamma_2(G_z, F_x)$ to $\Gamma_4(G_z, F_x)$, in turn corresponding to temperatures of 450 and 480 K, respectively. This region of spin-reorientation transition observed for SFO nanoparticles is in accordance with previous studies on SFO single crystals [9,20,46]. In order to understand the dielectric behavior of SFO nanoparticles around the spin-reorientation region and the effect of exchange striction associated to the region, as seen in the previous sections, we performed the dielectric measurements on SFO nanoparticles.

The origin of the dielectric constant is generally attributed to dipolar, interfacial, electronic, and ionic polarization. Increase of the dielectric constant at lower frequency and its dependency on temperature are usually due to interfacial polarization, while the behavior of the dielectric constant at higher frequencies and its dependency on temperature are attributed to electronic and ionic polarization [8]. Hence, the signatures of spin-phonon coupling and the impact of exchange striction driven magnetostriction can be reflected in the dielectric properties of the material. Figure 9(a) shows real permittivity vs temperature across the spin state transition, with a mild anomaly at T_{SR} and a relaxor-like behavior (frequency-dependent maxima in real permittivity) below the T_{SR} .

As seen from the $\epsilon'_\omega(T)$ plots at several frequencies [Fig. 9(a)], absence of a sharp feature at a fixed temperature (independent of frequency) rules out thermodynamic phase transition anew near T_{SR} . However, there exists a slope-break anomaly in the data at exactly $T_{SR} = 483$ K for each frequency. This is made quantitatively precise in the right panel [Fig. 9(b)], where $d\epsilon'/dT$ below and above T_{SR} are plotted at two typical radio frequencies. Finite discontinuities of the

T_{SR}^\pm slopes signify a subtle but sudden change of electrical character, brought about by the spin reorientation. Moreover, emergence of medium-range dipolar correlations manifests as dispersive $\omega_p(T)$ maxima in the dielectric constant below T_{SR} . The kinetics of this diffusive feature spanning some 50 K thermal window (400–450 K) is found to follow the Vogel-Fulcher-Tamman (VFT) behavior [Fig. 9(b) inset]; indicating divergence of the characteristic timescale $\tau(T) \sim 1/f_p(T)$ at finite $T_0 = 309$ K (right-panel inset). The VFT dependence of relaxation time is given by [47–49]

$$\tau = \tau_0 \exp\left(\frac{E_a}{T - T_0}\right) \quad (6)$$

where E_a is the activation of energy of the relaxation process, τ is the relaxation time, and T_0 is the freezing temperature for dipolar dynamics. This shows the vitreous character of the dipolar correlations, reflecting their medium-range length scale imposed by the microstructure of the present nanosynthesized compound. From the VFT fit, we also find the thermal activation energy $E_a = 158$ meV and the approach frequency f_0 of ~ 0.6 THz $\{\sim \tau^{-1}(T \rightarrow \infty)\}$ for the correlated dipolar dynamics. Noticing that no such diffusive or dispersive feature exists above T_{SR} , we infer that the lower- T , relaxor-like electrical organization is consequent to the prominent MEC realized in the spin-reconfigured state. Peculiar signatures in $\epsilon'_\omega(T)$ concur with the particulate features observed earlier in the structural and vibrational data [Figs. 3(c), 3(d); $B_{1g}(4)$, $B_{1g}(3)$ in Fig. 6(b); and $A_g(7)$, $B_{1g}(3)$ in Fig. 6(c)]. This is compelling for a crucial role of the tilt angles (Fe-O1-Fe and ϕ), bond lengths (Sm-O and Fe-O), FeO₆ bending and rotation, and Sm-O vibration in manifesting MEC effects below T_{SR} .

The smaller dielectric constant values obtained for our nanosynthesized specimen vis-à-vis large magnitudes reported

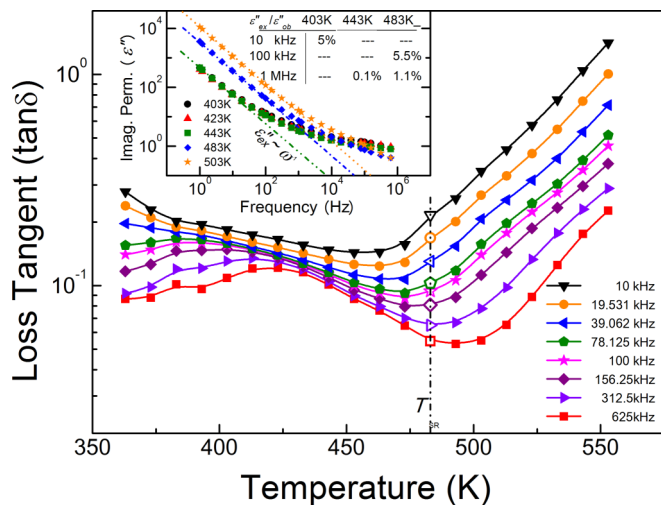


FIG. 10. Loss tangent ($\tan\delta$) as a function of temperature in the range 350 to 550 K for various frequencies. Inset shows imaginary permittivity (ϵ'') as a function of frequency recorded at various temperatures. Estimated extrinsic contributions to the measured data (tabulated in the inset) are under 6% at the relevant frequencies illustrating the anomaly at T_{SR} [Fig. 9(b)] and below [Fig. 9(a)].

for the bulk ceramics [20,23,50] are complemented by the consistently small losses, as shown in Fig. 9. However, the kinetics behavior is less delineable than that in the dielectric constant. Here, the low-valued and broadly humped feature at the lower temperature regime is distinguishable from the monotonic rise above, with a crossover around T_{SR} . The smaller permittivity is always closer to the intrinsic values, since the extrinsic contributions from intergrain, binder, and/or electrode-surface layers all tend to enhance both the dielectric constant and the losses. These thermally activated high-conductivity-driven extraneous responses due to local free charges dominate at low frequencies (less than kilohertz) and high temperatures [51–53]. Being from uncorrelated degrees of freedom, they feature purely Arrhenic kinetics that is impervious to any intragranular physical processes and transitions. For example, an electrical phase change or dipolar vitrification/short-range correlation can imprint its signature only in the intrinsic response. This is amply confirmed by the frequency-dependent imaginary permittivity $\epsilon''(\omega)$ in the inset of Fig. 10. Here, the extrinsic regime is marked by a high static conductivity ($\epsilon'' = \sigma_0/\epsilon_0\omega \sim \omega^{-1}$, straight lines), which extends up to higher frequencies at higher temperatures. Over the frequencies selected for the plots in Fig. 9, the ratio of the measured to extrinsic contribution ($\epsilon''/\epsilon''_{ext}$, Fig. 10 (inset)) increases from 20|_{10 kHz} to 900|_{1 MHz}, spread over some 40 K temperature window; corresponding to a decreasing extrinsic contribution from 5% at 10 kHz/403 K to 0.1% at 1 MHz/443 K. The same amounts to decreasing from 5.5%|_{100 kHz} to 1.1%|_{1 MHz} at exactly T_{SR} . Hence, both the electrical vitreousity (relaxor-like behavior) over 400–440 K [inset of Fig. 9(b)] and the slope discontinuity at T_{SR} in the T -dependent dielectric constant [Fig. 9(b)] witnessed in the present data are essentially the allied intrinsic signatures of the spin-reorientation transition.

The origin of the relaxor-like state in SFO nanoparticles below T_{SR} can be attributed to significant displacement of the

Sm ion within the lattice and Fe-Sm interaction giving rise to the exchange–striction (magnetoelastic) mechanism [21]. The onset of para- to ferroelectric transition around the AFM ordering temperature ($T_N = 670$ K) and a nonzero value of spontaneous polarization existing between T_N and T_{SR} (670 and 480 K) has been reported using density functional theory (DFT) and in single crystal of SFO by Lee *et al.* [20]. While contrasting our dielectric measurements with those reported by Kuo *et al.* (with the electric field along the b axis and the $Pbnm$ setting on a single crystal of SFO [23]), it is noted that (1) in the single crystal study, no anomaly was reported around T_{SR} or T_N and (2) no observation of relaxor ferroelectricity in dielectric properties of a single crystal of SFO has been reported.

The relaxor-like behavior below T_{SR} is induced by the canted AFM ordering in SFO nanoparticles. As discussed in the introduction, the mechanism proposed behind this observation is striction through the exchange interaction between Sm and Fe spins, which is reported for a single crystal of SFO at T_N , on the basis of theory and magnetic measurements [20,21,23]. This is also observed for other rare earth orthoferrite single crystals and bulk materials around T_N [45]. In the case of SFO nanoparticles in the present paper, the evidence of exchange striction between Sm and Fe ions is clearly and significantly observed at and below T_{SR} . This aspect has not been previously explored or observed.

IV. CONCLUSIONS

SFO nanoparticles (~ 65 nm) have been synthesized using a sol-gel route. Temperature-dependent XRD, Raman spectroscopy, and dielectric measurements around the spin-reorientation transition temperature viz. 480 K have been performed. Upon extensive analysis of synchrotron XRD and Raman spectroscopy data, an anomaly around T_{SR} is observed. The signature of unusual relaxor ferroelectric-like behavior in SFO nanoparticles around T_{SR} also has been found. The ED plots obtained using refinement of XRD data clearly support the observed changes. The origin of polarizability around T_{SR} can be attributed to significant displacement of the Sm ion within the lattice and the Fe-Sm interaction giving rise to an exchange striction (magnetoelastic) mechanism, which is contributing to the short-range relaxor ferroelectric-like behavior observed in SFO nanoparticles. Although the behavior and mechanism observed are agreeable with reports of single crystal and bulk, the direct and clear signatures observed here for SFO nanoparticles at T_{SR} have not been reported or studied for single crystal and bulk material. These findings are significant in understanding the structural changes taking place around spin-reorientation temperature (T_{SR}) and below Néel temperature (T_N), where SFO is AFM and shows a signature of improper ferroelectricity. Spin-reorientation transition above room temperature is useful for application in switching devices. Also, the contribution of this phenomenon of the change in structural parameters and presence of strong spin-phonon coupling, can be helpful in understanding the possibility of the existence of ferroelectricity and unusual dielectric behaviour in SFO nanoparticles. It would be interesting to study the dependence of T_{SR} on particle size in a nanoregime. The findings presented in this paper are interesting, because spin-reorientation transition above room temperature is useful

for application in switching devices, and the contribution of this phenomenon in a change in structural parameters, as well as the presence of strong spin-phonon coupling, can be helpful in understanding the possibility of the existence of ferroelectricity in the SFO nanoparticles.

ACKNOWLEDGMENTS

This work was carried out under the Department of Science and Technology, Ministry of Science and Technology Grant No. SR/WOS/-A/PS50/2012(G), India. The authors

sincerely acknowledge Dr. Surjeet Singh, Indian Institute of Science Education and Research, Pune, for providing magnetic measurements. The authors thank Dr. Vasant Sathe for the Raman spectroscopy measurements at the UGC-DAE Consortium for Scientific Research, Indore, India, and Anil Prathamshetti for FESEM micrographs. The authors also thank the Department of Science and Technology, India, for financial support through Project 2015-IB-05, and the Saha Institute of Nuclear Physics, India, for facilitating the synchrotron XRD experiments at the Indian Beamline, Photon Factory, KEK, Japan.

-
- [1] N. A. Hill, *J. Phys. Chem. B* **104**, 6694 (2000).
- [2] N. A. Hill and A. Filippetti, *J. Magn. Magn. Mater.* **245**, 976 (2002).
- [3] R. Saha, A. Sundaresan, and C. N. R. Rao, *Mater. Horizons* **1**, 20 (2014).
- [4] S. Hu, L. Chen, Y. Wu, L. Yu, X. Zhao, S. Cao, J. Zhang, and W. Ren, *Chin. Sci. Bull.* **59**, 5170 (2014).
- [5] G. V. Subba Rao, C. N. R. Rao, and J. R. Ferraro, *Appl. Spectrosc.* **24**, 436 (1970).
- [6] S. Venugopalan, M. Dutta, A. K. Ramdas, and J. P. Remeika, *Phys. Rev. B* **31**, 1490 (1985).
- [7] J. P. Remeika, *J. Am. Chem. Soc.* **78**, 4259 (1956).
- [8] K. Sultan, M. Ikram, and K. Asokan, *Vacuum* **99**, 251 (2014).
- [9] S. Cao, H. Zhao, B. Kang, J. Zhang, and W. Ren, *Sci. Rep.* **4**, 5960 (2014).
- [10] M. Abe, K. Kaneta, M. Gomi, Y. Mori, and S. Nomura, *Jpn. J. Appl. Phys.* **16**, 1799 (1977).
- [11] Z. Zhou, L. Guo, H. Yang, Q. Liu, and F. Ye, *J. Alloys Compd.* **583**, 21 (2014).
- [12] K. P. Belov, A. M. Kadomtseva, B. Krynetskii, T. L. Ovchinnikova, and V. A. Timofeeva, *Sov. Phys. JETP* **36**, 1136 (1973).
- [13] B. Berini, A. Fouchet, E. Popova, J. Scola, Y. Dumont, N. Franco, R. M. C. da Silva, and N. Keller, *J. Appl. Phys.* **111**, 053923 (2012).
- [14] N. A. Povahzynaja, I. G. Shvejtzer, and A. V. Soldatov, *J. Phys.: Condens. Matter* **7**, 4975 (1995).
- [15] Z. Cheng, F. Hong, Y. X. Wang, K. Ozawa, H. Fujii, H. Kimura, Y. Du, X. Wang, and S. X. Dou, *ACS Appl. Mater. Interfaces* **6**, 7356 (2014).
- [16] J. Fink-Finowicki, *Phys. Status Solidi (b)* **74**, K27 (1976).
- [17] L. Joly, F. Nolting, A. V. Kimel, A. Kirilyuk, R. V. Pisarev, and T. Rasing, *J. Phys.: Condens. Matter* **21**, 446004 (2009).
- [18] X. Fu, X. Zeng, D. Wang, H. Chi Zhang, J. Han, and T. Jun Cui, *Sci. Rep.* **5**, 14777 (2015).
- [19] Y. K. Jeong, J.-H. Lee, S.-J. Ahn, and H. M. Jang, *Solid State Commun.* **152**, 1112 (2012).
- [20] J.-H. Lee, Y. K. Jeong, J. H. Park, M.-A. Oak, H. M. Jang, J. Y. Son, and J. F. Scott, *Phys. Rev. Lett.* **107**, 117201 (2011).
- [21] J.-H. Lee, Y. K. Jeong, J. H. Park, M.-A. Oak, H. M. Jang, J. Y. Son, and J. F. Scott, *Phys. Rev. Lett.* **108**, 219702 (2012).
- [22] R. D. Johnson, N. Terada, and P. G. Radaelli, *Phys. Rev. Lett.* **108**, 219701 (2012).
- [23] C.-Y. Kuo, Y. Drees, M. T. Fernandez-Diaz, L. Zhao, L. Vasylechko, D. Sheptyakov, A. M. T. Bell, T. W. Pi, H.-J. Lin, M.-K. Wu, E. Pellegrin, S. M. Valvidares, Z. W. Li, P. Adler, A. Todorova, R. Küchler, A. Steppke, L. H. Tjeng, Z. Hu, and A. C. Komarek, *Phys. Rev. Lett.* **113**, 217203 (2014).
- [24] B. V. Prasad, G. Narsinga Rao, J. W. Chen, and D. Suresh Babu, *Mater. Res. Bull.* **46**, 1670 (2011).
- [25] Y. Tokunaga, S. Iguchi, T. Arima, and Y. Tokura, *Phys. Rev. Lett.* **101**, 097205 (2008).
- [26] Y. Tokunaga, N. Furukawa, H. Sakai, Y. Taguchi, T. Arima, and Y. Tokura, *Nat. Mater.* **8**, 558 (2009).
- [27] W. Li, H. Shen, and J. Xu, *J. Sol-Gel Sci. Technol.* **76**, 637 (2015).
- [28] S. Yuvaraj, S. Layek, S. M. Vidyavathy, S. Yuvaraj, D. Meyrick, and R. K. Selvan, *Mater. Res. Bull.* **72**, 77 (2015).
- [29] S. Chaturvedi, I. Sarkar, M. M. Shirolkar, U.-S. Jeng, Y.-Q. Yeh, R. Rajendra, N. Ballav, and S. Kulkarni, *Appl. Phys. Lett.* **105**, 102910 (2014).
- [30] S. Chaturvedi, M. M. Shirolkar, R. Rajendra, S. Singh, N. Ballav, and S. Kulkarni, *J. Appl. Phys.* **115**, 123906 (2014).
- [31] S. Chaturvedi, R. Das, P. Poddar, and S. Kulkarni, *RSC Adv.* **5**, 23563 (2015).
- [32] S. Chaturvedi, R. Bag, V. Sathe, S. Kulkarni, and S. Singh, *J. Mater. Chem. C* **4**, 780 (2016).
- [33] E. N. Maslen, V. A. Streltsov, and N. Ishizawa, *Acta Crystallogr. Sect. B Struct. Sci.* **52**, 406 (1996).
- [34] M. N. Iliev, M. V. Abrashev, H.-G. Lee, V. N. Popov, Y. Y. Sun, C. Thomsen, R. L. Meng, and C. W. Chu, *Phys. Rev. B* **57**, 2872 (1998).
- [35] M. J. Martínez-Lope, J. A. Alonso, M. Retuerto, and M. T. Fernández-Díaz, *Inorg. Chem.* **47**, 2634 (2008).
- [36] S. M. Selbach, J. R. Tolchard, A. Fossdal, and T. Grande, *J. Solid State Chem.* **196**, 249 (2012).
- [37] P. M. Woodward, *Acta Crystallogr. B* **53**, 44 (1997).
- [38] D. Sands, *Introduction to Crystallography* (Dover Publications, New York, 1993).
- [39] M. C. Weber, J. Kreisel, P. A. Thomas, M. Newton, K. Sardar, and R. I. Walton, *Phys. Rev. B* **85**, 054303 (2012).
- [40] S. Chanda, S. Saha, A. Dutta, and T. P. Sinha, *Mater. Res. Bull.* **48**, 1688 (2013).
- [41] V. S. Bhadram, B. Rajeswaran, A. Sundaresan, and C. Narayana, *Europhys. Lett.* **101**, 17008 (2013).
- [42] H. C. Gupta, Manoj Kumar Singh, and L. M. Tiwari, *J. Raman Spectrosc.* **33**, 67 (2002).

- [43] E. Granado, A. García, J. A. Sanjurjo, C. Rettori, I. Torriani, A. Caneiro, F. Prado, R. D. Sánchez, and S. B. Oseroff, *Phys. Rev. B* **60**, 11879 (1999).
- [44] M. Mochizuki, N. Furukawa, and N. Nagaosa, *Phys. Rev. B* **84**, 144409 (2011).
- [45] Y. Tokura, S. Seki, and N. Nagaosa, *Rep. Prog. Phys.* **77**, 076501 (2014).
- [46] L. G. Marshall, J.-G. Cheng, J.-S. Zhou, J. B. Goodenough, J. Q. Yan, and D. G. Mandrus, *Phys. Rev. B* **86**, 064417 (2012).
- [47] H. Vogel, *Physik Z.* **22**, 645 (1921).
- [48] G. S. Fulcher, *J. Am. Ceram. Soc.* **8**, 339 (1925).
- [49] Z. G. Tammann and G. Hesse, *Anorg. Allg. Chem.* **156**, 245 (1926).
- [50] S. Sahoo, P. K. Mahapatra, and R. N. P. Choudhary, *J. Phys. D: Appl. Phys.* **49**, 035302 (2016).
- [51] P. Lunkenheimer, V. Bobnar, A. V. Pronin, A. I. Ritus, A. A. Volkov, and A. Loidl, *Phys. Rev. B* **66**, 052105 (2002).
- [52] G. Catalan, *Appl. Phys. Lett.* **88**, 102902 (2006).
- [53] S. Pandey, J. Kumar, and A. M. Awasthi, *J. Phys. D: Appl. Phys.* **47**, 435303 (2014).